GPR Uncertainty Modelling and Analysis of Object Depth based on Constrained Least-square

Fei XIE[1], Wallace W.L. Lai[1, *], Xavier Dérobert [2]

[1]Department of Land Surveying and Geo-informatics, The Hong Kong Polytechnic University, Hong Kong
[2]Université Bretagne-Loire, IFSTTAR, Centre de Nantes, 44344, Bouguenais, France

[*]Email: wallace.wai.lok.lai@polyu.edu.hk

Abstract

The development of ground penetrating radar (GPR) in recent decades has promoted the role of this popular near-surface geophysical detection method. A step further is its use from a prospecting tool of approximate estimation of location of buried objects to an accurate survey equipment which then involves understanding of measurement errors/uncertainties. This paper firstly discussed the sources of uncertainty of object depth's measurements with respect to host material, instrumentation, data collection method and signal processing. We modelled these sources of errors by formulating computation sets based on applying constrained least-square algorithm on hyperbolic reflections arisen from buried objects. Based on the computation, uncertainty analysis was performed through (1) identification of errors on measurements of hyperbolic reflections and (2) conducting error propagation for evaluating the combined uncertainty of surveyed depth. At a geophysical test site at IFSTTAR, Nantes, France, sets of control experiments were conducted to validate the proposed uncertainty analysis method and to investigate the correlation between the evaluated uncertainty and the factors of host material, center frequency of antenna, the depth of target and the horizontal and vertical resolution in the radargram. Several conclusions were made as follows. Firstly, the uncertainty of the centimeter-order of the survey results can be achieved for depth estimation of objects at several meters deep at ±2 standard deviation at a 95% confidence interval. Secondly, errors of time zero location at different GPR center frequency dominate the evaluation of the uncertainty while the resolution of radargram and the noise from scattering doesn't explicitly affect the evaluated uncertainty.

Key words: uncertainty, depth estimation, GPR, least square

1. Introduction

Ground penetrating radar (GPR), as a well-developed near-surface geophysical method, is getting more and more popular for the surveying and mapping of underground utilities. With a common-offset setting antenna, GPR signal transmitted by the transmitter of antenna, penetrates into underground, spreads downwards in a conical form, and then reflected back when encountering objects with significant dielectric contrast to the host materials (Daniels, 2004; Jol, 2009). The reflected signal is received by the receiver of antenna. As GPR antenna is towed across the target pipe along the traverse, it's obvious that the distance between the antenna and the target becomes shorter from position x_i to position x_0. Hence, such curved reflection is formed in radargrams as illustrated in figure 1.

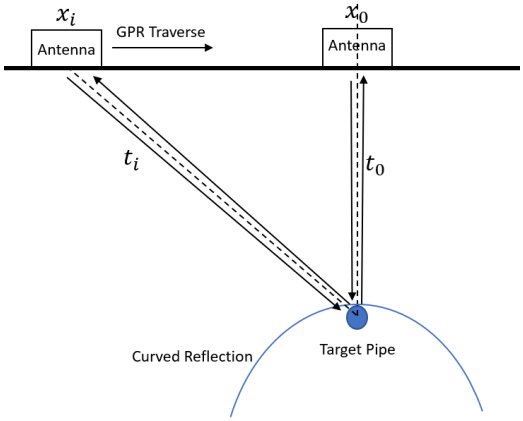

Figure 1 Model of GPR wave travel path (antenna and target as point source)

Based on this curved reflection, diverse algorithms are proposed and studied to estimate the GPR wave velocity and the depth of the target pipe (ASTM, 2011; Ristic, et al., 2009; Sham & Lai, 2016; Shihab & Al-Nuaimy, 2005; Xie, et al., 2018). Subsequently, the uncertainties of this estimation results become an inevitable discussion and require rising attention to be paid from researchers. On the contrary, limited attention (Jacob & Hermance, 2005; Solla, et al., 2013; Wu et al., 2003) has been drawn on this issue. Standards and specifications from various countries and regions (Anspach, 2002; Australia, 2013; CJJ, 2003; HKIUS, 2012, 2014; ICE, 2014; Malaysia, 2006) provide guidelines for GPR operation. But accuracies are rarely mentioned for GPR survey results except PAS 128 (ICE, 2014). This specification suggests an accuracy of 40% or 15% of the detected depth in different quality levels. But these requirements came from the perception of the practitioners and the clients without scientific evidence which bias cannot be avoided. To reduce bias, errors of the estimated object depth by GPR can be established with uncertainty/error propagation models. First step of which is to identity the sources of uncertainties which are host material, instrumentation, data collection method and signal processing.

I. Host material, where the target is buried, has significant effects on the GPR wave's propagation as the electromagnetic wave is sensitive to the dielectric property and water content of the propagation medium (Topp, et al., 1980; Chan & Knight, 2001; Hugenschmidt & Loser, 2008; Huisman, et al., 2003; Klysz & Balayssac, 2007; Lai, er al., 2011a, 2011b; Lai, et al., 2012; Lai, et al., 2006; Lai, et al., 2010; Lai, et al., 2010; Lai, et al., 2014; Lai, 2006). The heterogeneity of host material also affects the scattering of EM wave and introduce unpredictable noise into the curved reflection resulting from the target pipe (Nielsen, et al., 2010; Takahashi, et al., 2011, 2012).

II. Instrumentation: various antenna designs will result in the difference of the GPR wave travel paths. Those paths require appliable algorithms to be adopted for velocity and depth

estimation, for example the mono-static antenna (Lambot, et al., 2004; Lambot, et al., 2004) and the bi-static antennas including common-offset setting (Sham & Lai, 2016; Xie, et al., 2018), common mid-point (Jacob & Urban, 2016; Steelman & Endres, 2012) and wide angle reflection (Galagedara, et al., 2005; Klysz, et al., 2004). The center frequency of the antenna is also so crucial as the electric and magnetic properties of GPR wave are always frequency dependent (Lai, et al., 2011).

III. Data collection method: during data acquisition, the parameters setting (time window, scans/meter and samples/A-scan) determines the digital sampling of the odometer and radio signals. They are controlled by sampling resolutions which appear in the horizontal and vertical axis in the radargram. Better resolution in radargrams is believed to lead to less error in measurements with regard to the distances (horizontal axis) and two-way travel times (vertical axis). Also, the included angle between the GPR traverse and the target pipe alignment also changes the shape of the reflection pattern resulting from the target (Xie, et al., 2018).

IV. Signal processing: several algorithms for velocity and depth estimation are developed by many researchers to promote the accuracy of survey results by GPR (Sham & Lai, 2016; Xie, et al., 2018). Further, the definition of time-zero is the most critical in the GPR survey (Lai et al., 2010; Yelf, 2004) as it concerns all measurements of GPR signal's two-way travel time.

After identifying the sources of errors, GUM (JCGM, 2008) and Shi (2009) can be referred for quantitative error analysis. Remaining content of this paper will first briefly introduce the model to estimate the depth of target pipe by GPR. Secondly, errors in the depth estimation will be analyzed and evaluated. Thirdly, results of validation experiments will be reported an discussed to verify the method of the uncertainty analysis.

2. Modelling GPR wave travel path according to observation of pairs of displacement and travel time measurement

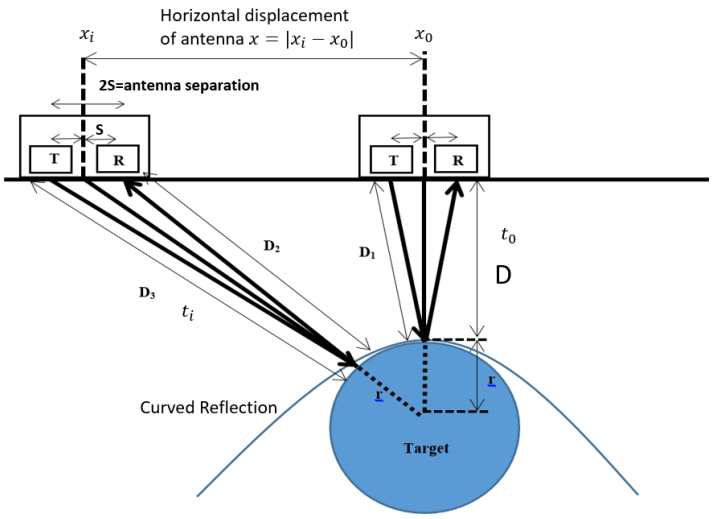

Figure 2 Refined model of GPR wave travel path

When the target is out of the Fresnel zone, GPR wave travels in ray path form. Figure 1 presents a typical model of that path when common offset setting antenna is utilized for surveying (ASTM, 2011). This model is popularly adopted in commercial software of signal processing

for velocity and depth estimation. But, the disadvantages of this model are obviously the too simple assumption about both the antenna and the target pipe as point source. In other words, the antenna separation between transmitter and receiver and the radius of the target are ignored to simplify the trigonometry for calculation. When either the antenna separation or the target radius is of comparable magnitude relative to the cover depth of the target pipe, such ignorance will lead to significant errors in estimation results.

The model in figure 2 considers both the antenna separation and the radius of the cylindrical target. Solving the complex trigonometry among position x_i, position x_0 and the center of the target pipe, following polynomial equation (2-1) can be established (Sham & Lai, 2016; XIE, et al., Under Review; Xie, et al., 2018):

$$v^4 t_i^4 - 4v^2 {t_i}^2 * \left(\left(\sqrt{(D_0 + r)^2 + x^2} - r\right)^2 + S^2\right) + 16S^2 x^2 \left(1 - \frac{r}{\sqrt{(D + r)^2 + x^2}}\right) = 0 \quad (2\text{-}1)$$

$$D = \sqrt{\left(\frac{vt_0}{2}\right)^2 - S^2} \quad (2\text{-}2)$$

$$f_i[(x_i, t_i); (v, x_0, t_0); (S, r)]|_{i=1\ldots n} = 0 \quad (2\text{-}3)$$

where v is the GPR wave travel velocity, x is the antenna displacement from position x_i to position x_0, t_i, t_0 are the two-way travel time when the GPR antenna is respectively at position x_i and x_0, S is half of the antenna separation, r is the radius of the target pipe, and D is the cover depth.

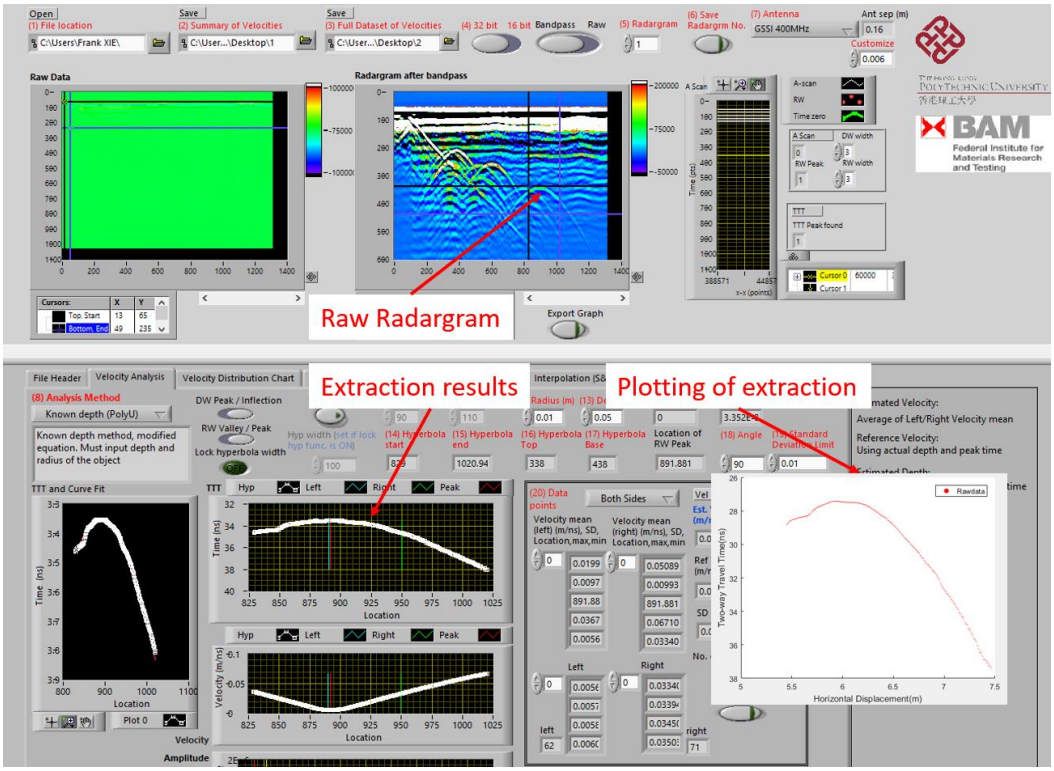

Figure 3 Interface of the inhouse built LabView program

An easier representation in functional format is provided as the non-linear equation (2-3). All concerned parameters are divided into 3 groups. $(x_i, t_i)|_{i=1\ldots n}$ are the observations which can be directly extracted from the curved reflection resulting from the target pipe by an inhouse

built LabVIEW program (Sham & Lai, 2016). The interface of the in-house built LabVIEW program is presented in Figure 3, as well as the plotting of the extracted $(x_i, t_i)|_{i=1\dots n}$. (S, r) are assumed to be known before survey. S, the half of the antenna separation is usually indicated by the specification of the antenna from the producer. r, the radius of the cylindrical target pipe can be referred to the as-built record. (v, x_0, t_0) which indicates wave velocity (v) travelled above the target pipe at position (x_0, t_0) are the variables to be estimated. Then, based on which the cover depth can be calculated according to equation (2-2).

The solution of the non-linear relationship in equation (2-3) is done in two steps:

I. Approximation of the non-linear equation (2-3) through first-order Taylor expansion.

$$f[(x_i, t_i); (v, x_0, t_0)] \approx A(W + w) + B(U_0 + u) \tag{2-4}$$

$$\text{Let} \begin{cases} \underset{2n*1}{W} = (x_1, t_1, x_2, t_2, \dots, x_n, t_n)^T \\ \underset{2n*1}{w} = (\Delta x_1, \Delta t_1, \Delta x_2, \Delta t_2, \dots, \Delta x_n, \Delta t_n)^T \end{cases} \tag{2-5}$$

$$\text{And let} \begin{cases} \underset{3*1}{U} = (v,\ x_0,\ t_0)^T = U_0 + u \\ \underset{3*1}{U_0} = (v^0, x_0^0, t_0^0)^T \\ \underset{3*1}{u} = (\Delta v,\ \Delta x_0,\ \Delta t_0)^T \end{cases} \tag{2-6}$$

Both (S, r) are assumed to be known and constant before survey, they are therefore excluded from the variables in the expansion. $U_0 = (v^0, x_0^0, t_0^0)^T$ in equation (2-6) are the initial values of the variables $U = (v,\ x_0,\ t_0)^T$, that require to be offered for Taylor expansion in advance. To guarantee the first-order Taylor expansion to be a good enough approximation, the initial values (U_0) should be provided as accurate as possible. As more accurate the initial values of U_0 are, the smaller the correction matrix $u = (\Delta v,\ \Delta x_0,\ \Delta t_0)^T$ will be and thus, the higher orders of the correction are small enough to be ignored. The velocity estimation method ($v = 2|x_i - x_0|/\sqrt{t_i^2 - t_0^2}$) from ASTM can be adopted for the determination of the initial value v^0. (x_0^0, t_0^0) represents the shortest two-way travel time ($\min_{i=1\dots n} t_i$) at the apex of the any curved reflection and the corresponding x_i directly. Substituting equation (2-3) into (2-4),

$$\begin{gathered} Aw + Bu + F_0 = 0 \\ \text{where } \underset{n*1}{F_0} = -AW - BU_0 \end{gathered} \tag{2-7}$$

A and B are the first-order derivatives as the coefficient matrix in Taylor expansion, as presented in equation (2-8).

$$\underset{n*2n}{\mathrm{A}} = \begin{pmatrix} \frac{\partial f_1}{\partial x_1} & \frac{\partial f_1}{\partial t_1} & 0 & 0 & & 0 \\ 0 & 0 & \frac{\partial f_2}{\partial x_2} & \frac{\partial f_2}{\partial t_2} & & \\ & & & & \ddots & \vdots \\ & 0 & & & \cdots & \frac{\partial f_n}{\partial x_n}\ \frac{\partial f_n}{\partial t_n} \end{pmatrix};\ \underset{n*3}{\mathrm{B}} = \begin{pmatrix} \frac{\partial f_1}{\partial v} & \frac{\partial f_1}{\partial x_0} & \frac{\partial f_1}{\partial t_0} \\ \frac{\partial f_2}{\partial v} & \frac{\partial f_2}{\partial x_0} & \frac{\partial f_2}{\partial t_0} \\ \vdots & \vdots & \vdots \\ \frac{\partial f_n}{\partial v} & \frac{\partial f_n}{\partial x_0} & \frac{\partial f_n}{\partial t_0} \end{pmatrix} \tag{2-8}$$

II. Constrained least-square solution of the approximation in step I.

Equation (2-7) is an inconsistent equation set (2*n inputs $(x_i, t_i)|_{i=1\dots n}$ that constructs 'n' equations $f_i[(x_i, t_i); (v^0, x_0^0, t_0^0)]|_{i=1\dots n} = 0$ to solve for 2*n+3 variables in w and u). To solve this inconsistent equation set, least-square fitting is introduced to minimize the square of

the Euclidean distance of the correction matrix w in equation (2-9). Blue scattering dots are the extracted $(x_i, t_i)|_{i=1\ldots n}$ and the red curve is the model to be fitted in Figure 4.

$$\begin{cases} \mathrm{Aw} + \mathrm{Bu} + F_0 = 0 \\ min \sum_{i=1}^{n} (\Delta x_i^2 + \Delta t_i^2) = w^T \mathrm{w} = \min \end{cases} \tag{2-9}$$

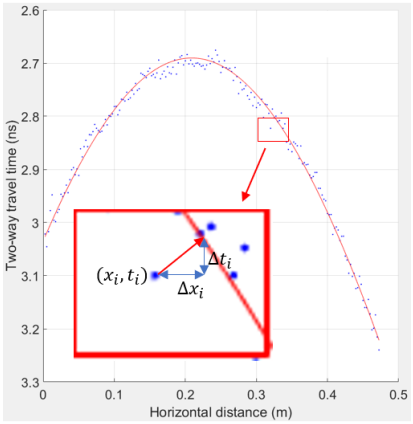

Figure 4 Euclidean distance based least-square

Equation (2-9) represents a constrained least-square problem (the least-square $w^T \mathrm{w} = \min$ with an equality constraint $\mathrm{Aw} + \mathrm{Bu} + F_0 = 0$). For solution, Lagrange multiplier K can be introduced to construct a new function as:

$$g = \underset{1*2n}{w^T} * \underset{2n*1}{w} - 2\underset{1*n}{K}(\underset{n*2n}{\mathrm{A}} * \underset{2n*1}{w} + \underset{n*3}{\mathrm{B}} * \underset{3*1}{\mathrm{u}} + \underset{n*1}{F_0}) \tag{2-10}$$

Because of $\mathrm{Aw} + \mathrm{Bu} + F_0 = 0$, the solution for the least-square $w^T \mathrm{w} = \min$ must be the stationary point of function g, as the value of g also reaches the minimum. According to the definition of the stationary point of a function, where the first-order derivatives should be equal to zero, the following equation (2-11) can be established.

$$\begin{cases} \dfrac{\partial g}{\partial w} = 2\underset{1*2n}{w^T} - 2\underset{1*n}{K} * \underset{n*2n}{\mathrm{A}} = 0 \\ \dfrac{\partial g}{\partial u} = -2\underset{1*n}{K} * \underset{n*3}{\mathrm{B}} = 0 \end{cases} \tag{2-11}$$

Equation (2-11) is a consistent equation set and the unique solution can be obtained. Then after solving the Lagrange multiplier K, the solution of the correction matrix w and u for the constrained least-square problem can be developed as equations (2-12) and (2-13).

$$\begin{cases} u = [B^T(AA^T)^{-1}B]^{-1}[-B^T(AA^T)^{-1}F_0] = NF_0 \\ w = -A^T(AA^T)^{-1}(Bu + F_0) \end{cases} \tag{2-12}$$

$$U = (v,\ x_0,\ t_0)^T = U_0 + u = (v^0, x_0^0, t_0^0)^T + (\Delta v,\ \Delta x_0,\ \Delta t_0)^T \tag{2-13}$$

3. Uncertainty/error propagation

Equation (2-3) implies that the (x_i, t_i) are the inputs and the (v, x_0, t_0) are the three variables to be estimated for depth measurement. This section studies how the errors propagate from the

inputs (x_i, t_i) to the three variables (v, x_0, t_0) and to the estimated depth according to equation (2-2).

3.1. Uncertainties/errors from observation

Observations x_i are the displacements of antenna when it travels along the traverse, which is determined directly from radargrams. The key factor that dictates the errors in observed x_i is the horizontal resolution (scans/meter). For example, if the scans/meter is set as 100, the actual value of x_i is assumed to be equally distributed within $x_i \pm \frac{1}{2} * \frac{1m}{100}$. Such error is subjected to the rectangular distribution of equal probability of values between the upper and lower bound. Half of the rectangular distribution bound can be denoted as $RD_{half\ bound|x_i} = \frac{1}{2} * \frac{1m}{100}$. GUM (JCGM, 2008) instructs the calculation of the observational standard deviation of such error as:

$$O\_\sigma_{x_i} = \frac{RD_{half\ bound|x_i}}{\sqrt{3}} \tag{3-1}$$

Because of the independency of measuring each $x_i|_{i=1\ldots n}$, the observational covariance between arbitrary $x_i|_{i=1\ldots n}$ and $x_j|_{j=1\ldots n}$ are equal to zero.

$$O\_\sigma_{x_i x_j}|_{i\neq j; i,j=1\ldots n} = 0 \tag{3-2}$$

The indirect determination of two-way travel time t_i is completed by two steps. Firstly, the time of reflection event is directly picked as τ_{t_i} from the radargram. Secondly, the time-zero τ_0 when the GPR signal penetrates the ground surface needs to be defined in A-scan. The two-way travel time can then be calculated by equation (3-3).

$$t_i = \tau_{t_i} - \tau_0 \tag{3-3}$$

The error of picked τ_{t_i} is decided by the vertical resolution of the radargram. Two factors are involved: the length of time window and the setting of 'samples/scan' which is the sampling rate of the vertical axis. Similar to the derivation in x_i, taking 1024 samples/scan as example, half of the rectangular distribution bound of τ_{t_i} is $RD_{half\ bound|\tau_{t_i}} = \frac{1}{2} * \frac{time\ window\ (ns)}{1024\ smaples/scan}$. And the calculation of corresponding observational standard deviation $O\_\sigma_{\tau_{t_i}}$ can refer to equation (3-1).

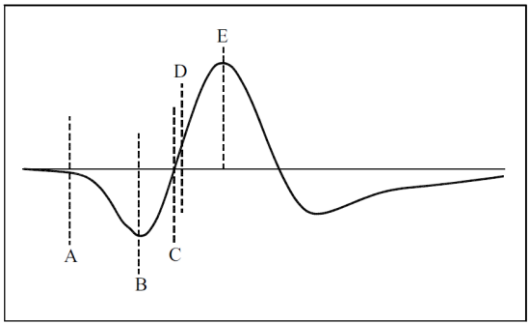

Figure 5 Time-zero in A-scan waveform of GPR signal (Yelf, 2004)

As far as the error of defining time zero τ_0 is concerned, there is no agreement about the exact position of true time zero in the GPR waveform (Yelf, 2004). It's assumed that the true time

zero may be allocated from the first break point (point A in figure 3) to the first positive apex (point E) of the first wave (direct wave) in A-scan with equal possibility. In other words, the interval from point A to point E defines the bound of the rectangular distribution for the error of defining the time-zero. Hence, the standard deviation can be evaluated by equation (3-4).

$$\sigma_{\tau_0} = \frac{(\frac{\tau_E - \tau_A}{2})}{\sqrt{3}} \tag{3-4}$$

The calculation in equation (3-3) implies the dependency between $t_i|_{i=1\dots n}$ and $t_j|_{j=1\dots n}$ because the time-zero τ_0 are always concerned. Their correlation can be represented in below matrix form.

$$(t_i, t_j)^T = \begin{pmatrix} 1 & 0 & -1 \\ 0 & 1 & -1 \end{pmatrix} * \begin{pmatrix} \tau_{t_i} \\ \tau_{t_j} \\ \tau_0 \end{pmatrix} = C \begin{pmatrix} \tau_{t_i} \\ \tau_{t_j} \\ \tau_0 \end{pmatrix} \tag{3-5}$$

Appling the error propagation law of variance and covariance, the observational variance-covariance matrix of $t_i, t_j|_{i\neq j;i,j=1\dots n}$ can be derived as:

$$\begin{aligned} O\_Var_{(t_i,t_j)^T} &= \begin{pmatrix} O\_\sigma_{t_i}^2 & O\_\sigma_{t_i t_j} \\ O\_\sigma_{t_i t_j} & O\_\sigma_{t_j}^2 \end{pmatrix} \\ &= C * \begin{pmatrix} O\_\sigma_{\tau_{t_i}}^2 & 0 & 0 \\ 0 & O\_\sigma_{\tau_{t_j}}^2 & 0 \\ 0 & 0 & O\_\sigma_{\tau_0}^2 \end{pmatrix} * C^T = \begin{pmatrix} O\_\sigma_{\tau_{t_i}}^2 + \sigma_{\tau_0}^2 & \sigma_{\tau_0}^2 \\ \sigma_{\tau_0}^2 & O\_\sigma_{\tau_{t_i}}^2 + O\_\sigma_{\tau_0}^2 \end{pmatrix} \end{aligned} \tag{3-6}$$

It's apparent in equation (3-6) that the observation variance of t_i is $O\_\sigma_{t_i}^2 = O\_\sigma_{\tau_{t_i}}^2 + \sigma_{\tau_0}^2$ and the observational covariance of $t_i, t_j|_{i\neq j;i,j=1\dots n}$ is $O\_\sigma_{t_i t_j} = \sigma_{\tau_0}^2$.

3.2. Uncertainties/errors from scattering

The least-square in figure 4 indicates that the raw observations (x_i, t_i) (red scattering dots) need to be corrected by a correction matrix w to fit the model established (red curve in Figure 4). This correction matrix w is also a kind of error that will be propagated to the final estimated depth, which is mainly caused by the scattering of the host material on the GPR signal.

If the host material is scattering-free, all the measured raw observations (x_i, t_i) should perfectly match the model established in equation (2-3). In other words, the expectation for all the $\Delta x_i, \Delta t_i$ in correction matrix w is equal to zero. Further, in equation (2-3), at least 3 x_i and 3 t_i should be offered to solve the 3 variables of (v, x_0, t_0), which means the degree of freedom for $\Delta x_i|_{i=1\dots n}$ and that for $\Delta t_i|_{i=1\dots n}$ are $(n-3)$.

According to the definition of variance, the uncertainties from scattering can be evaluated as:

$$S\_\sigma_{x_i} = \sqrt{\frac{\sum_{i=1}^{n}(\Delta x_i - 0)^2}{n-3}} \tag{3-7}$$

$$S\_\sigma_{t_i} = \sqrt{\frac{\sum_{i=1}^{n}(\Delta t_i - 0)^2}{n-3}} \tag{3-8}$$

Because the observational errors and the errors from scattering are independent, the variance and covariance of (x_i, t_i) can be combined as:

$$\sigma_{x_i}^2 = O\_{\sigma_{x_i}}^{\ 2} + S\_{\sigma_{x_i}}^{\ 2} \tag{3-9}$$

$$\sigma_{t_i}^2 = O\_{\sigma_{t_i}}^{\ 2} + S\_{\sigma_{t_i}}^{\ 2} \tag{3-10}$$

$$\sigma_{t_i t_j} = O\_\sigma_{t_i t_j} = \sigma_{\tau_0}^2 \tag{3-11}$$

Back referring to equation (2-5), the covariance matrix of the observation W can be constructed.

$$\underset{2n*2n}{Var_{WW}} = \begin{pmatrix} \sigma_{x_1}^2 & \sigma_{x_1 t_1} & \sigma_{x_1 x_2} & \sigma_{x_1 t_1} & & \sigma_{x_1 x_n} & \sigma_{x_1 t_n} \\ \sigma_{t_1 x_1} & \sigma_{t_1}^2 & \sigma_{t_1 x_2} & \sigma_{t_1 t_2} & & \sigma_{t_1 x_n} & \sigma_{t_1 t_n} \\ \sigma_{x_2 x_1} & \sigma_{x_2 t_1} & \sigma_{x_2}^2 & \sigma_{x_2 t_2} & & \sigma_{x_2 x_n} & \sigma_{x_2 t_n} \\ \sigma_{t_2 x_1} & \sigma_{t_2 t_1} & \sigma_{t_2 x_2} & \sigma_{t_2}^2 & & \sigma_{t_2 x_n} & \sigma_{t_2 t_n} \\ & & & & \ddots & & \\ \sigma_{x_n x_1} & \sigma_{x_n t_1} & \sigma_{x_n x_2} & \sigma_{x\ t_2} & & \sigma_{x_n}^2 & \\ \sigma_{t_n x_1} & \sigma_{t_n t_1} & \sigma_{t_n x_2} & \sigma_{t_n t_2} & & & \sigma_{t_n}^2 \end{pmatrix} = \begin{pmatrix} \sigma_{x_1}^2 & 0 & 0 & 0 & & 0 & 0 \\ 0 & \sigma_{t_1}^2 & 0 & \sigma_{\tau_0}^2 & & 0 & \sigma_{\tau_0}^2 \\ 0 & 0 & \sigma_{x_2}^2 & 0 & & 0 & 0 \\ 0 & \sigma_{\tau_0}^2 & 0 & \sigma_{t_2}^2 & & 0 & \sigma_{\tau_0}^2 \\ & & & & \ddots & & \\ 0 & 0 & 0 & 0 & & \sigma_{x_n}^2 & \\ 0 & \sigma_{\tau_0}^2 & 0 & \sigma_{\tau_0}^2 & & & \sigma_{t_n}^2 \end{pmatrix} \tag{3-12}$$

3.3. Propagation of the errors/uncertainties

In equations (2-6) and (2-13), U_0 is the initial values to be offered in advance to perform the first-order Taylor expansion and is hence assumed as constant with no errors. Then the variances of F_0 and of U can be propagated.

$$Var_{F_0 F_0} = A * Var_{WW} * A^T \tag{3-13}$$

$$Var_{UU} = Var_{uu} \tag{3-14}$$

Applying error propagation law to equation (2-12) and then combining with equations (3-13) and (3-14), following can be derived.

$$Var_{uu} = N * Var_{F_0 F_0} * N^T \tag{3-15}$$

$$Var_{UU} = \begin{pmatrix} \sigma_{vv}^2 & \sigma_{vx_0} & \sigma_{vt_0} \\ \sigma_{vx_0} & \sigma_{x_0 x_0}^2 & \sigma_{x_0 t_0} \\ \sigma_{vt_0} & \sigma_{x_0 t_0} & \sigma_{t_0 t_0}^2 \end{pmatrix} = Var_{uu} \tag{3-16}$$

According to equation (2-2), the first-order derivatives of the cover depth relative to the GPR wave velocity v and relative to the variable t_0 can be derived as the coefficients for the error propagation of the estimated cover depth.

$$Var_{DD} = \begin{pmatrix} \frac{\partial D}{\partial v} & \frac{\partial D}{\partial t_0} \end{pmatrix} * \begin{pmatrix} \sigma_{vv}^2 & \sigma_{vt_0} \\ \sigma_{vt_0} & \sigma_{t_0 t_0}^2 \end{pmatrix} * \begin{pmatrix} \frac{\partial D}{\partial v} & \frac{\partial D}{\partial t_0} \end{pmatrix}^T \tag{3-17}$$

4. Validation experiments

Three sets of control experiments were carried out on the geophysical test site (figure 6) at IFSTTAR, Nantes, France to validate the proposed method of uncertainty analysis in section 3 (Derobert & Pajewski, 2018; Dérobert & Pajewski, 2018).

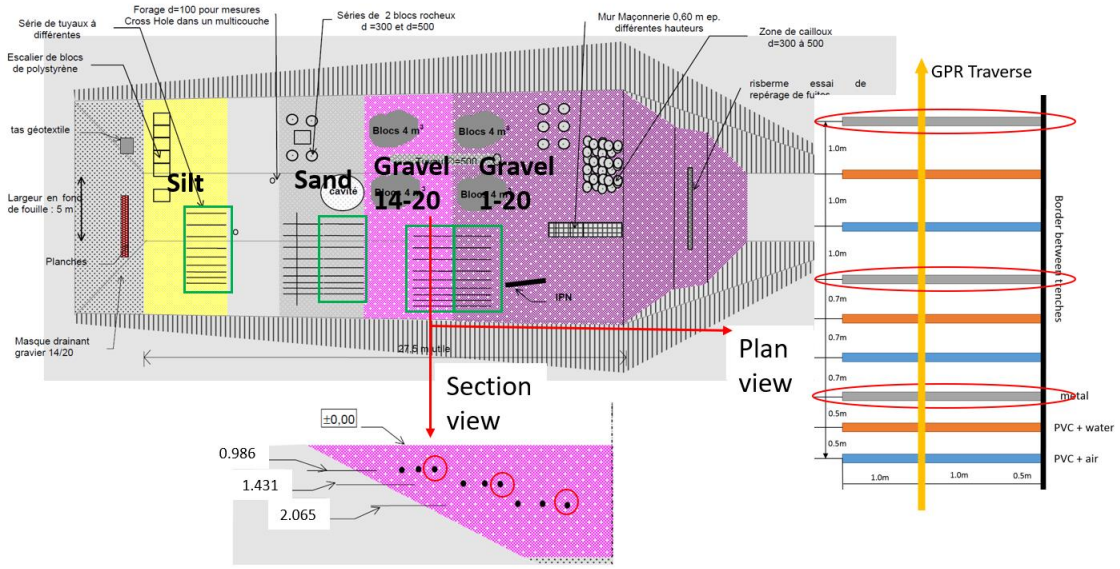

Figure 6 Geophysical test site at IFSTTAR, Nantes, France

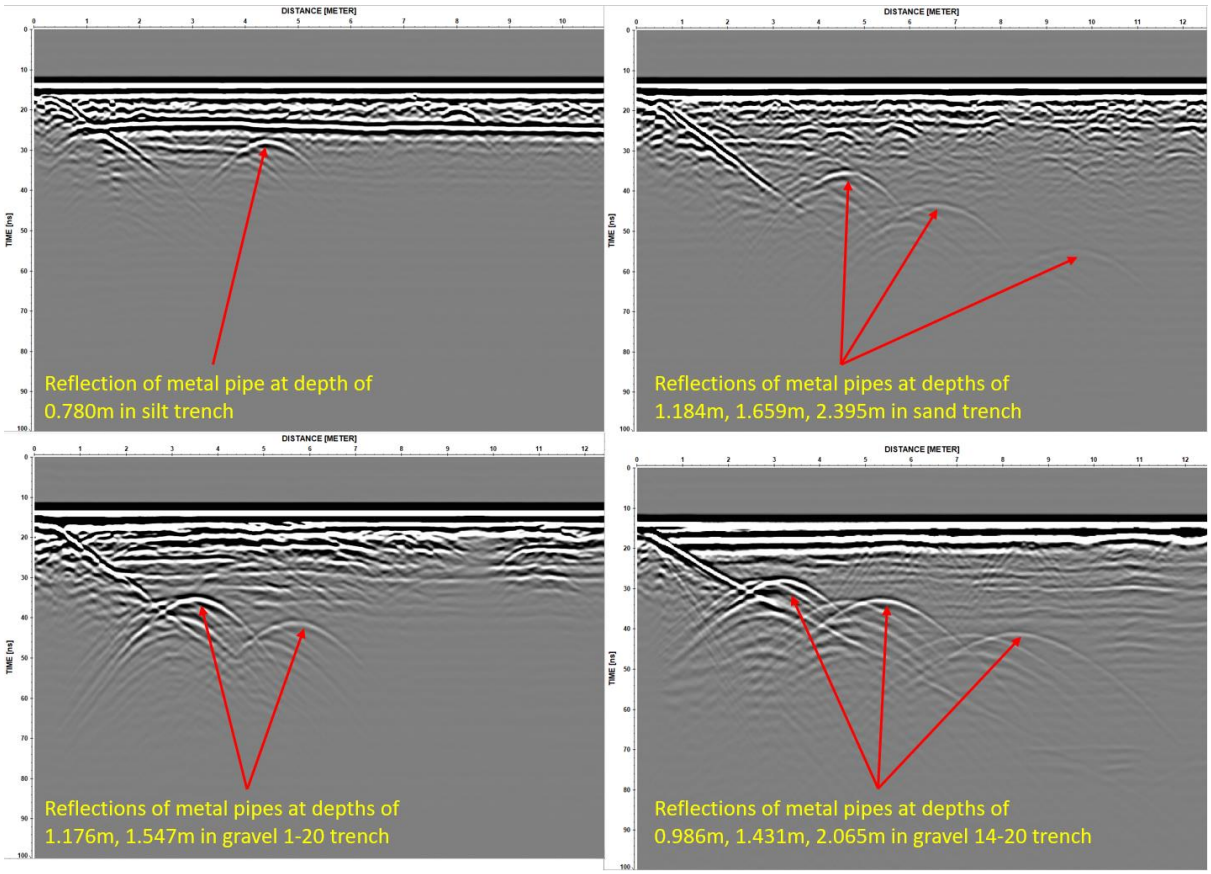

Figure 7 Reflections from metal pipes of 400MHz antenna

Four trenches were excavated and backfilled with silt, sand, gravel with nominal size of aggregates ranging from 1-20mm (namely 'gravel 1-20' or well-graded soil) and 14-20mm (namely 'gravel 14-20', or coarse gravel), respectively. In every trench, 9 pipes (3 metal pipes, 3 PVC pipes filled with water and 3 PVC pipes filled with air) were buried in the green rectangular area. The horizontal and vertical layout of the 9 pipes are presented in the 'Plan view' and the 'Section view' in figure 6. The three metal pipes in each trench (circled by red in figure 6) were selected as the target because of their significant dielectric contrast to the host material and the strong reflections in radargrams. The GPR traverses followed the yellow arrow in 'Plan view' to acquire radargrams and were always kept perpendicular to the alignment of the pipes.

First set of experiments were conducted on the gravel 14-20 trench. GSSI common offset antenna of center frequencies at 200MHz, 270MHz, 400MHz, 500MHz and 900MHz were used for data collection with GSSI 4000 control unit. Those reflections were extracted as (x_i, t_i). Then the cover depth was estimated and corresponding uncertainty (standard deviation) was also evaluated following the method suggested in previous section (table 1).

	Freq.	Actual D. (m)	V (m/ns)	SD of V (m/ns)	D(m)	|Error| (m)	|Error| (%) (m)	SD of D (m)	Standard score
Gravel 14-20	200M	0.986	0.136	0.0049	0.890	0.096	10.8	0.0711	-1.35
		1.431	0.155	0.0055	1.413	0.018	1.3	0.0671	-0.27
		2.065	0.148	0.0031	1.970	0.095	4.8	0.0713	-1.33
	270M	0.986	0.121	0.0053	0.835	0.151	18.1	0.0390	-3.88
		1.431	0.156	0.0044	1.435	0.004	0.3	0.0527	0.08
		2.065	0.157	0.0016	2.120	0.055	2.6	0.0764	0.72
	400M	0.986	0.145	0.0037	1.018	0.032	3.1	0.0404	0.79
		1.431	0.149	0.0028	1.408	0.023	1.7	0.0406	-0.58
		2.065	0.150	0.0019	2.049	0.016	0.8	0.0436	-0.36
	500M	0.986	0.143	0.0039	1.018	0.032	3.2	0.0803	0.40
		1.431	0.148	0.0039	1.418	0.013	0.9	0.0375	-0.34
		2.065	0.149	0.0019	2.054	0.011	0.6	0.0511	-0.22
	900M	0.986	0.144	0.0026	0.985	0.001	0.1	0.0240	-0.06
		1.431	0.147	0.0015	1.366	0.065	4.7	0.0339	-1.91

Table 1 Results of trench gravel 14-20

Column '|Error (m)|' records the absolute difference between the estimated depth D and the actual depth while column '|Error (%) (m)|' is the percentage of the absolute error over the estimated depth. Similar to the normalization procedure of a Gaussian distribution, the 'Standard score' is calculated according to below equation (4-1). As the evaluated standard deviations are relative to various buried depths of pipes, this normalization can help to regress all the evaluated uncertainties to an identical scale for easier later inter-comparison among them and for statistical purpose. For example if $|Standard\ score| \leq 2$, it represents that the actual depth of the target pipe falls in the range of the estimated depth $\pm 2 * SD$.

$$Standard\ score = \frac{Estimated\ \ D - Actual\ D}{Standard\ Deviation\ of\ Estimated\ D} \tag{4-1}$$

Second set of experiments used the GSSI common offset antennas of 270MHz, 400MHz and 900MHz towed over the trenches of well-graded gravel 1-20mm, sand and silt. Typical radargrams were presented in figure 7 from 400MHz antenna with clear curved reflections. The experimental results are listed in table 2. Because of the severe attenuation and absorption of host materials (i.e. silt) and the shallower penetrating depth of GPR signal from higher frequency antenna (i.e. 900MHz), the reflections from some deeper pipes were either not detected by the GPR or too weak to be recognized and extracted from the radargrams. Thus,

those results were missed in table 2. Especially for the silt trench, only the results of the shallowest metal pipe can be obtained.

	Freq.	Actual D. (m)	V (m/ns)	SD of V (m/ns)	D(m)	|Error| (m)	|Error| (%) (m)	SD of D (m)	Standard score
Gravel 0-20	270M	1.176	0.118	0.0021	1.260	0.084	6.6	0.0460	1.82
		1.547	0.115	0.0020	1.584	0.037	2.3	0.0381	0.98
	400M	1.176	0.118	0.0015	1.266	0.090	7.1	0.0306	2.93
		1.547	0.112	0.0015	1.532	0.015	1.0	0.0235	-0.63
	900M	1.176	0.107	0.0017	1.139	0.037	3.2	0.0226	-1.64
Sand	270M	1.184	0.117	0.0031	1.266	0.082	6.5	0.0344	2.39
		1.659	0.121	0.0013	1.810	0.151	8.3	0.0536	2.82
		2.395	0.102	0.0011	2.094	0.301	14.4	0.0537	-5.60
	400M	1.184	0.115	0.0022	1.232	0.048	3.9	0.0216	2.22
		1.659	0.110	0.0006	1.744	0.085	4.9	0.0288	2.94
		2.395	0.112	0.0025	2.259	0.136	6.0	0.0349	-3.89
	900M	1.184	0.116	0.0015	1.234	0.050	4.1	0.0319	1.57
Silt	270M	0.780	0.112	0.0034	0.771	0.009	1.2	0.0405	-0.23
	400M	0.780	0.112	0.0025	0.776	0.004	0.6	0.0233	-0.19

Table 2 Results of gravel 1-20, sand and silt trenches

Last set of experiments were conducted with gravel 14-20 trench using 400MHz antenna but with various parameters settings (time window, scans/meter, samples/scan) for comparison. It's a replication of the first set experiments. Table 3 and table 4 list the specific settings of those three parameters and corresponding details of experimental results, respectively.

	Time Window (ns)	Scans/m	Samples/Scan
Setting1	100	100	1024
Setting2	100	200	2048
Setting3	100	200	512

Table 3 Specific setting of parameters

	Settings	Actual D. (m)	V (m/ns)	SD of V (m/ns)	D(m)	|Error| (m)	|Error| (%) (m)	SD of D (m)	Standard score
Gravel 14-20	Setting1	0.986	0.145	0.0037	1.018	0.032	3.1	0.0404	0.79
		1.431	0.149	0.0028	1.408	0.023	1.7	0.0406	-0.58
		2.065	0.150	0.0019	2.049	0.016	0.8	0.0436	-0.36
	Setting2	0.986	0.139	0.0032	0.954	0.032	3.4	0.0413	-0.78
		1.431	0.150	0.0030	1.414	0.017	1.2	0.0385	-0.43
		2.065	0.155	0.0015	2.119	0.054	2.5	0.0493	1.10
	Setting3	0.986	0.136	0.0042	0.940	0.046	4.9	0.0341	-1.34
		1.431	0.149	0.0028	1.397	0.034	2.5	0.0405	-0.85
		2.065	0.151	0.0026	2.056	0.009	0.5	0.0330	-0.28

Table 4 Results of various parameters settings of trench gravel 14-20 (400MHz)

5. Discussion

5.1. Effects of the host materials

To investigate the effects of the host materials, the observational error and the error from defining the time-zero (section 3.1) in (x_i, t_i) are ignored first. Only the error from scattering (section 3.2) is considered and propagated to evaluate the uncertainties. Those evaluated standard deviations of 270MHz and 400MHz antennas are then averaged regarding to the four trenches, despite the various depths of the target pipes (table 5 and figure 8). The standard deviations of 900MHz are excluded from this average calculation due to the shallow penetration depth and limited data obtained, especially in silt trench that even the shallowest metal pipe can't be detected (referring to table 2).

Average SD (Scattering error only) (m)		
Host Material	270MHz	400MHz
Gravel 1-20	0.0030	0.0042
Gravel 14-20	0.0142	0.0079
Sand	0.0179	0.0078
Silt	0.0033	0.0025

Table 5 Specific values of standard deviations (scattering error only) of various trenches

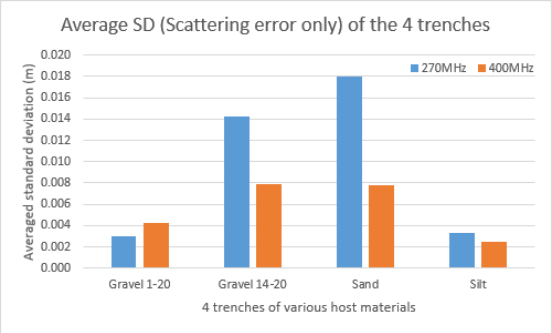

Figure 8 Column chart of average standard deviations (scattering error only) of various trenches

Figure 8 implies that the evaluated uncertainties for the pipes buried in gravel 14-20 trench and in sand trench are higher than these for the pipes buried in trenches of gravel 1-20 and silt, and not related to antenna frequency. From the description of the host materials, the particles sizes of silt trench and of gravel 1-20 trench are generally smaller than those in trenches of gravel 14-20 and sand. Larger particle sizes in trenches of gravel 14-20 and sand represent that the scattering between the host material and the GPR signal shifts from Rayleigh scattering to Mie scattering. In other words, Rayleigh scattering introduces less noises into the reflection data resulting from the target pipe, which lead to smaller uncertainties in the estimation results. But as a trade-off, shallower penetration depth will be achieved in small-particle trenches (gravel 1-20 and silt) because of severer signal attenuation.

5.2. Effects of the antenna center frequencies

Furthermore, the evaluated standard deviations are also averaged regarding to the antenna frequency. Averaged results are summarized in table 6. Figure 9 plots all the averaged standard deviations in column chart categorized by the center frequencies of the antennas.

	Average standard deviation (m)			
Center frequency	Gravel 14-20	Gravel 1-20	Sand	Silt
200MHz	0.0698			
270MHz	0.0560	0.0421	0.0472	0.0405
400MHz	0.0415	0.0271	0.0284	0.0233
500MHz	0.0563			
900MHz	0.0290	0.0226	0.0319	
900MHz (Scattering error only)	**0.0066**	**0.0141**	**0.0220**	

Table 6 Specific values of average standard deviations of various antennas

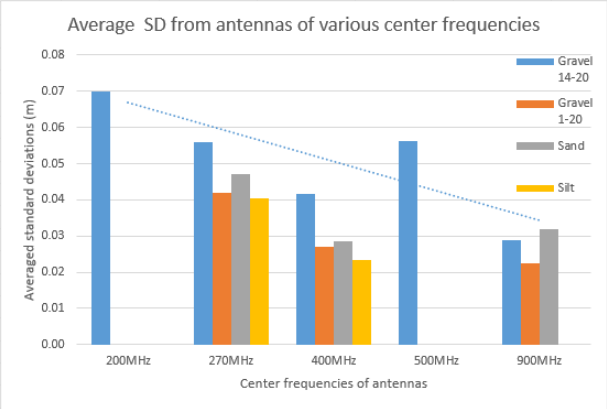

Figure 9 Column chart of average SD in terms of various antennas

The trend line (blue dash) in figure 9 explicitly indicates that in each trench, as the center frequency of antenna used for data collection increases, the evaluated standard deviation of the results decreases, except that of 500MHz antenna on gravel 14-20 trench. This is because the wavelength of higher frequency component is shorter than that of lower frequency. The uncertainty of time-zero in figure 3 implies that shorter wavelength can result in narrower rectangular bound for the error from defining the time-zero (specific widths of the rectangular bounds are identified in A-scan and listed in table 7). When the horizontal and vertical resolutions in radargrams are identical, which means the errors from the system digitization in observations (x_i, t_i) are constant, the errors from defining the time-zero dictate the evaluation of the uncertainty while the scattering errors are not of comparable magnitude. Hence, the decline of standard deviation resulting from the increasing of the antenna center frequency appears in figure 9 as the errors from defining the time-zero is decreased.

	Rectangular bound of time-zero (ns)			
Center frequency	Gravel 14-20	Gravel 1-20	Sand	Silt
200MHz	5.2			
270MHz	4.1	3.9	4.0	3.9
400MHz	3.1	2.7	2.7	2.5
500MHz	3.5			
900MHz	2.0	1.9	1.9	

Table 7 The width (ns) of the rectangular bound defined in A-scan for time-zero

Transferring the column chart in figure 9 to line chart, following figure 10 is plotted by excluding the cases of 200MHz and 500MHz antennas. We can discover that the decline trend of evaluated standard deviations as the increase of antenna center frequencies is slighted compensated in the cases of gravel 1-20 trench comparing to that in gravel 14-20 trench. And for the cases in sand trench, the evaluated uncertainty of 900MHz is even larger than that of 400MHz. This is because the scattering errors from 900MHz antenna are comparable to the evaluated combined uncertainties (considering all the errors from radargram resolution, time-zero definition and scattering), especially for sand trench (referring to the values in the last row in table 6).

Hence, the tradeoff is revealed that as the center frequency of antenna rises, the error from defining time-zero decreases but the error from scattering increases. And both of them will impact the combined uncertainty of surveyed depth.

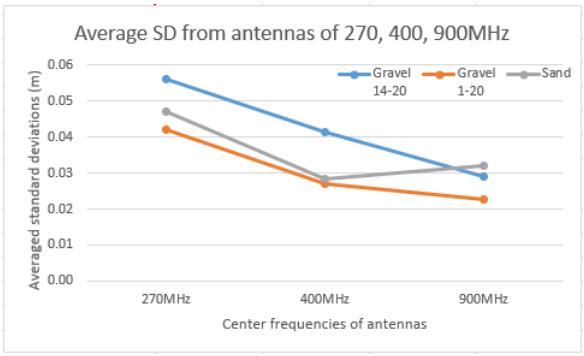

Figure 10 Line chart of averaged SD in terms of various antennas

5.3. Effects of the object depths

Empirically, the tolerance of the survey results by GPR is positively proportional to the depth of the target in industrial underground utility survey (XIE & LAI, Under Review), just like the accuracy requirement in PAS 128 is defined as a percentage (40% or 15%) of the detected depth. The obvious reason is that for deeper target pipes, the GPR signal needs to travel longer distance and hence, more scattering happens between the wave and the host material. The experimental data in this study also substantiates this empirical judgement. Taking the results from sand trench as an example, the errors from scattering only are analyzed and propagated with respect to the pipes at various depths. The line chart in figure 11 evidently supports that deeper target pipe will lead to high level of scattering noise and result in bigger evaluated standard deviations. But this phenomenon is not applicable to the combined uncertainty because of the effects of errors from radargram resolution and from time-zero definition.

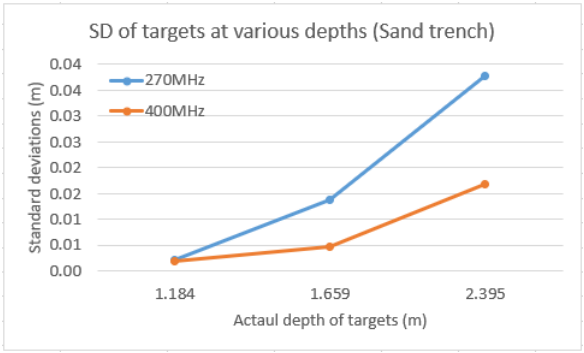

Figure 11 Standard deviation of pipes at various depths in sand trench

5.4. Effects of the horizontal and vertical resolution of GPR measurements

The error analysis in section 3 reveals that theoretically, the better resolution in horizontal and vertical axis in radargrams will lead to higher accuracy of the estimated depth because of narrower rectangular distribution bound and smaller errors in observations (x_i, t_i). However, the evaluation results in the third set of control experiments doesn't support this theoretical conclusion. Referring to the data in table 4, the standard deviations from setting2 (best resolution in table 3) are not always the smallest relative to those from setting1 and setting3. A further calculation was completed to investigate the underlying reason of this phenomenon.

	Settings	Actual D. (m)	SD of D (m)	SD2 of D (m) (Sampling error only)
Gravel 14-20	Setting1	0.986	0.0394	0.0035
		1.431	0.0403	0.0022
		2.065	0.0424	0.0053
	Setting2	0.986	0.0406	0.0017
		1.431	0.0385	0.0008
		2.065	0.0487	0.0014
	Setting3	0.986	0.0336	0.0060
		1.431	0.0404	0.0028
		2.065	0.0392	0.0028

Table 8 Calculated standard deviations with and without considering the errors of defining time-zero

In table 8, the last column 'SD2 of D' records the calculated standard deviations without considering the errors of defining time-zero ($\sigma_{\tau_0} = 0$ in equation (3-4)) and the errors from scattering while the column 'SD of D' is filled with the standard deviations evaluated following the normal procedure in section 3. Comparing those values, it's obvious that the evaluated standard deviations (at the order of centimeters) in column 'SD of D' are significantly larger than those in column 'SD2 of D' (at the order of millimeters). Therefore, although the standard deviations in column 'SD2 of D' from Setting2 are smaller than those from Setting1 and Setting3 (this is consistent with the theoretical analysis), the difference of the parameters settings in table 3 doesn't significantly influences the final results of the combined standard deviation.

5.5. Statistical analysis of the standard score

In terms of the standard score in tables 1, 2 and 4, statistical analysis was performed. Because all the standard scores of sand trench are extremely high (the absolute values of those standard scores are larger than 2), they are excluded from the statistical analysis. The occurrence of the standard scores within each pre-defined interval is showed in table 9, as well as the probability (the percentage of the frequency corresponding to each interval over the population, the amount of experiment cases). The histogram is also drawn in figure 12 based on the statistical data in table 9.

Interval of Normalized SD	Frequency	Interval of Normalized SD	Probability
(-∞,-3)	1	[-1,1]	70%
[-3,-2)	0		
[-2,-1)	5	[-2,2]	93%
[-1,1]	21		
(1,2]	2	[-3,3]	96%
(2,3]	1		
(3,+∞)	0		

Table 9 Statistical analysis of normalized standard deviations

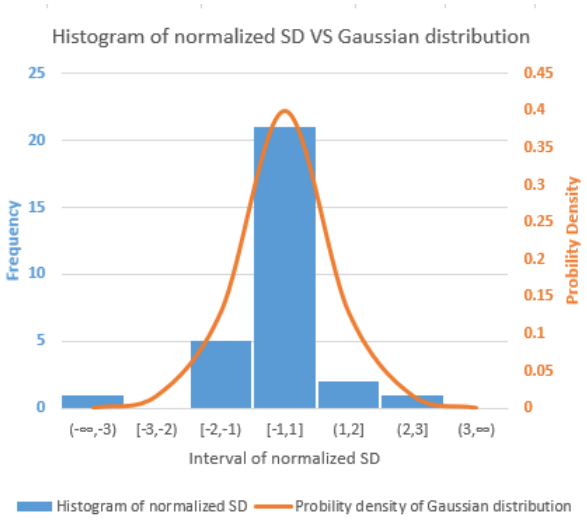

Figure 12 Histogram of normalized standard deviations VS Gaussian distribution

According to the normalization calculation in equation (4-1), the intervals of the standard scores '[-1,1]' '[-2,2]' and '[-3,3]' correspond to that the actual depth of the target pipe is within the estimated depth $\pm SD$, $\pm 2 * SD$ and $\pm 3 * SD$, respectively. Referring to the Gaussian distribution $y \sim (\bar{y}, \sigma^2)$, the probabilities of coverage $|y - \bar{y}| \leq \sigma, 2\sigma, 3\sigma$ are 68%, 95% and 99%, respectively. Comparing those probabilities with the values in table 9, we found the similarity between the distribution of the standard scores and the Gaussian distribution. The match between the histogram in figure 12 and the probability density function of a normal Gaussian distribution (orange curve) also proves this. So far, it's reasonable to conclude the evaluated uncertainty of the estimated cover depth by GPR is subjected to a Gaussian distribution.

6. Conclusion

1) The uncertainty of the measured depth of the underground pipe by GPR (target buried at depth 1-3 meters) can achieve the order of several centimeters. What's more, considering the 40% or 15% of detected depth as the accuracy requirement in PAS 128, the overall average percentage of the absolute error over the estimated depth in tables 1, 2 and 4 is only 3.9%. Such quality and reliability are high enough for industrial underground utility survey, which means that GPR can also play the role of an accurate survey equipment in terms of underground surveying and mapping rather than just a prospecting tool.
2) Generally speaking, the center frequency of common offset setting antenna dominates the uncertainty evaluation of GPR survey results. Higher frequency of antenna will lead to a more accurate survey result, although the scattering noise from high frequency antenna may slightly degrade such survey results. This can also instruct the instrumentation selection before conducting GPR survey. After considering the trade-off between the antenna frequency and the maximum penetration depth which should cover the buried depth of target, antenna of as much as high center frequency should be adopted for data collection, not only for better resolution of imaged radargram, but also for more reliable survey results.
3) Attention should not be paid to the parameters setting of the scans/meter and samples/scan. Better horizontal and vertical resolution in radargram doesn't provide either better precision (smaller difference between estimated depth and the actual depth) or higher accuracy (smaller standard deviation) in estimation results, but expand the volume of data collected and slow down the speed of data collection. Therefore, the efficiency of the data acquisition should be the first concern for setting those parameters in industrial survey.

4) Defining the true time-zero accurately is with significant importance for the combined uncertainty evaluation of GPR survey results.
5) The 95% confidence interval is believed to be constructed as $\pm 2 * SD$ for the survey results of GPR as the uncertainty of the estimated depth is sensibly assumed to be subjected to the Gaussian distribution.

Reference

Anspach, J. H. (2002). *Standard guideline for the collection and depiction of existing subsurface utility data.* Paper presented at the Pipelines 2002: Beneath Our Feet: Challenges and Solutions.

ASTM, D. (2011). Standard Guide for Using the Surface Ground Penetrating Radar Method for Subsurface Investigation. In.

Australia, S. (2013). Classification of subsurface utility information (SUI). In. Standards Australia.

Chan, C. Y., & Knight, R. J. (2001). Laboratory measurements of electromagnetic wave velocity in layered sands. *Water resources research, 37*(4), 1099-1105.

CJJ, C. (2003). 城市地线管线探测技术规程. In *CJJ 61-2003*: CJJ China.

Daniels, D. J. (2004). *Ground penetrating radar* (Vol. 1): Iet.

Derobert, X., & Pajewski, L. (2018). *The GPR dataset of the IFSTTAR Geophysical Test Site.* Paper presented at the EGU General Assembly Conference Abstracts.

Dérobert, X., & Pajewski, L. (2018). TU1208 open database of radargrams: The dataset of the IFSTTAR geophysical test site. *Remote Sensing, 10*(4), 530.

Galagedara, L., Parkin, G., Redman, J., Von Bertoldi, P., & Endres, A. (2005). Field studies of the GPR ground wave method for estimating soil water content during irrigation and drainage. *Journal of Hydrology, 301*(1-4), 182-197.

HKIUS. (2012). Guide to utility survey by non-destructive method (using pipe/cable locator) in hong kong. In: HK: Utility Training Institute.

HKIUS. (2014). Particular specification for utility mapping by non-destructive methods. In. HKIUS-UT PS: HK: Utility Training Institute.

Hugenschmidt, J., & Loser, R. (2008). Detection of chlorides and moisture in concrete structures with ground penetrating radar. *Materials and Structures, 41*(4), 785-792.

Huisman, J., Hubbard, S., Redman, J., & Annan, A. (2003). Measuring soil water content with ground penetrating radar. *Vadose zone journal, 2*(4), 476-491.

ICE. (2014). PAS 128: British standard: Specification for underground utility detection, verification and location In *British standard: Specification for underground utility detection, verification and location* British Standard Institute: Institute of Civil Engineer

Jacob, R. W., & Hermance, J. F. (2005). Random and non-random uncertainties in precision GPR measurements: Identifying and compensating for instrument drift. *Subsurface Sensing Technologies and Applications, 6*(1), 59-71.

Jacob, R. W., & Urban, T. (2016). Ground-penetrating radar velocity determination and precision estimates using common-midpoint (CMP) collection with hand-picking, semblance analysis and cross-correlation analysis: a case study and tutorial for archaeologists. *Archaeometry, 58*(6), 987-1002.

JCGM. (2008). Evaluation of measurement data—Guide to the expression of uncertainty in measurement. *JCGM*.

Jol, H. M. (2009). *Ground Penetrating Radar Theory and Applications*: Oxford: Elsevier.

Klysz, G., & Balayssac, J.-P. (2007). Determination of volumetric water content of concrete using ground-penetrating radar. *Cement and Concrete Research, 37*(8), 1164-1171.

Klysz, G., Balayssac, J. P., & Laurens, S. (2004). Spectral analysis of radar surface waves for non-destructive evaluation of cover concrete. *NDT & E International, 37*(3), 221-227. doi:10.1016/j.ndteint.2003.09.006

Lai, W., Kind, T., & Wiggenhauser, H. (2011a). Frequency-dependent dispersion of high-frequency ground penetrating radar wave in concrete. *NDT & E International, 44*(3), 267-273.

Lai, W., Kind, T., & Wiggenhauser, H. (2011b). Using ground penetrating radar and time–frequency analysis to characterize construction materials. *NDT & E International, 44*(1), 111-120.

Lai, W., Kou, S., & Poon, C. (2012). Unsaturated zone characterization in soil through transient wetting and drying using GPR joint time–frequency analysis and grayscale images. *Journal of Hydrology, 452*, 1-13.

Lai, W., Tsang, W., Fang, H., & Xiao, D. (2006). Experimental determination of bulk dielectric properties and porosity of porous asphalt and soils using GPR and a cyclic moisture variation technique. *Geophysics, 71*(4), K93-K102.

Lai, W. L., Kind, T., & Wiggenhauser, H. (2010). A study of concrete hydration and dielectric relaxation mechanism using ground penetrating radar and short-time Fourier transform. *EURASIP Journal on Advances in Signal Processing, 2010*, 12.

Lai, W. L., Kind, T., & Wiggenhauser, H. (2010). A Study of Concrete Hydration and Dielectric Relaxation Mechanism Using Ground Penetrating Radar and Short-Time Fourier Transform. *EURASIP Journal on Advances in Signal Processing, 2010*(1), 317216. doi:10.1155/2010/317216

Lai, W. L., Kind, T., & Wiggenhauser, H. (2011). Frequency-dependent dispersion of high-frequency ground penetrating radar wave in concrete. *NDT & E International, 44*(3), 267-273. doi:10.1016/j.ndteint.2010.12.004

Lai, W. W.-L., Kind, T., Kruschwitz, S., Wöstmann, J., & Wiggenhauser, H. (2014). Spectral absorption of spatial and temporal ground penetrating radar signals by water in construction materials. *NDT & E International, 67*, 55-63.

Lai, W. W. L. (2006). Characterization of porous construction materials using electromagnetic radar wave.

Lambot, S., Rhebergen, J., Van den Bosch, I., Slob, E., & Vanclooster, M. (2004). Measuring the soil water content profile of a sandy soil with an off-ground monostatic ground penetrating radar. *Vadose zone journal, 3*(4), 1063-1071.

Lambot, S., Slob, E., van den Bosch, I., Stockbroeckx, B., Scheers, B., & Vanclooster, M. (2004). Estimating soil electric properties from monostatic ground-penetrating radar signal inversion in the frequency domain. *Water resources research, 40*(4).

Malaysia, N. (2006). Standard guideline for underground utility mapping. In: National Mapping and Spatial Data Committee.

Nielsen, L., Looms, M. C., Hansen, T. M., Cordua, K. S., & Stemmerik, L. (2010). Estimation of chalk heterogeneity from stochastic modeling conditioned by crosshole GPR traveltimes and log data. *Advances in near-surface seismology and ground-penetrating radar: SEG Geophysical Development Series, 15*, 379-398.

Ristic, A. V., Petrovacki, D., & Govedarica, M. (2009). A new method to simultaneously estimate the radius of a cylindrical object and the wave propagation velocity from GPR data. *Computers & Geosciences, 35*(8), 1620-1630.

Sham, J. F. C., & Lai, W. W. L. (2016). Development of a new algorithm for accurate estimation of GPR's wave propagation velocity by common-offset survey method. *NDT and E International, 83*, 104-113. doi:10.1016/j.ndteint.2016.05.002

Shi, W. (2009). *Principles of modeling uncertainties in spatial data and spatial analyses*: CRC press.

Shihab, S., & Al-Nuaimy, W. (2005). Radius estimation for cylindrical objects detected by ground penetrating radar. *Subsurface Sensing Technologies and Applications, 6*(2), 151-166.

Solla, M., González-Jorge, H., Lorenzo, H., & Arias, P. (2013). Uncertainty evaluation of the 1 GHz GPR antenna for the estimation of concrete asphalt thickness. *Measurement, 46*(9), 3032-3040.

Steelman, C. M., & Endres, A. L. (2012). Assessing vertical soil moisture dynamics using multi-frequency GPR common-midpoint soundings. *Journal of Hydrology, 436*, 51-66.

Takahashi, K., Igel, J., & Preetz, H. (2011). Clutter modeling for ground-penetrating radar measurements in heterogeneous soils. *IEEE Journal of Selected Topics in Applied Earth Observations and Remote Sensing, 4*(4), 739-747.

Takahashi, K., Igel, J., & Preetz, H. (2012). Modeling of GPR clutter caused by soil heterogeneity. *International Journal of Antennas and Propagation, 2012*.

Topp, G. C., Davis, J., & Annan, A. P. (1980). Electromagnetic determination of soil water content: Measurements in coaxial transmission lines. *Water resources research, 16*(3), 574-582.

Wu, R., Gu, K., Li, J., Bradley, M., Habersat, J., & Maksymonko, G. (2003). Propagation velocity uncertainty on GPR SAR processing. *IEEE Transactions on Aerospace and Electronic Systems, 39*(3), 849-861.

XIE, F., & LAI, W. W. L. (Under Review). GPR Uncertainty Modelling and Analysis of Object Depth based on Single Trilateration of Ray-paths.

XIE, F., Lai, W. W. L., & Dérobert, X. (Under Review). GPR-based Depth Measurement of Buried Objects based on Constrained Least-square Fitting Method of Reflections.

Xie, F., Sham, J. F.-C., Lai, W. W.-L., & Dérobert, X. (2018). *A modified algorithm for accurate GPR wave velocity estimation with common offset setting antenna.* Paper presented at the 2018 17th International Conference on Ground Penetrating Radar (GPR).

Xie, F., Wu, C. G.-W., Lai, W. W.-L., & Sham, J. F.-C. (2018). Correction of multi-frequency GPR wave velocity with distorted hyperbolic reflections from GPR surveys of underground utilities. *Tunnelling and Underground Space Technology, 76*, 76-91.

Yelf, R. (2004). *Where is true time zero?* Paper presented at the Proceedings of the Tenth International Conference on Grounds Penetrating Radar, 2004. GPR 2004.